NUMERICAL INVESTIGATION OF INLET DISTORTION INDUCED SWIRL IN MULTISTAGE FANS

Aspi R. Wadia*, Jixian Yao, Steve. E. Gorrell*****
***GE Aviation, **GE Global Research, ***Air Force Research Lab, WPAFB**
***30 Merchant Street, Princeton Hill P20, Cincinnati, Ohio 45246**

Keywords: *Multistage Fans, Inlet Distortion, Swirl*

Abstract

This paper presents a CFD analysis of flow swirl distortion induced by total pressure distortion and total temperature distortion for two multi-stage fans. The numerical simulations and analyses include the front block of the first fan, and the rear block of the second fan. The front block of the first fan is subject to a one/rev total pressure distortion, while the rear block of the second fan has both total pressure and total temperature distortions. The analyses of swirl generation and transfer behavior across the computational domain are discussed.

1 Introduction

Fielded compression components of aircraft engines seldom run in a uniform inlet flow field. Ever since the early days of aircraft engine installations, the effects of distorted inflow and incoming turbulence to gas turbine engines have been a concern. This concern is more pronounced as increasingly advanced aircraft are being designed for a wide range of operations and high fuel efficiency. Inlet distortion influences engine stability, performance, and structural integrity and is manifested by an inability to accelerate, engine overheating, compressor stall and surge, or combustion flame out. The engine must work with and tolerate the inlet distortion since it cannot be completely eliminated due to aircraft installation effects. The need for distortion-tolerant or distortion-insensitive fan design methodology requires an understanding of the flow physics that governs distortion transfer and sensitivity and is the major driving force of the current study. Inflow conditions are usually categorized into two classes, one is the steady-state, circumferential and/or radial variation of flow, and the other is the so-called dynamic distortion where the flow is time-variant. For circumferential distortion, the total pressure distortion, especially the per-rev type, has been studied and modeled the most.[1, 2, 3, 4, 5, 6, 7, 8, 9] The effect of total temperature distortion has been observed in military installations, such as weapon hot gas ingestion, vertical take-off and landing, steam ingestion during aircraft carrier operations, and mid-air refueling (gas leakage consumed by the fan). In recent years, the swirl distortion has been identified as the third major flow distortion initiator beside total pressure and total temperature distortions.[10, 11, 12, 13] The inlet swirl distortion can be generated by flight maneuvering and flow conditions near the aircraft. For commercial airplanes, congested air traffic at busy airports causes swirl (i.e. taking off after inlet distortion of total temperature and total pressure). The nacelle droop can sometimes cause inlet swirl distortion as well. For high-performance applications, components with serpentine inlets generate swirl as well at the fan face even if the inlet flow is uniform. Different patterns and scales of swirl distortion, such as buck swirl, peak swirl, and vortex swirl, have different effects on the rotating compression system.[14] In addition to stability concerns, vortex flow can set up a harmonic content in the flow field that could result in high-cycle fatigue. Furthermore, the three major distortion sources are related with each other in

a highly nonlinear fashion. For example, the time variance of static pressure causes total temperature to change, which could produce commensurate change in total pressure. Swirl changes can affect both total pressure and temperature.

Over the last decade, a great wealth of insights of unsteady flow physics in gas turbine engines was gained through experiments and computational fluid dynamics (CFD). As the capability of parallel computing and processor speed has increased steadily numerical simulations play an increasingly important role in discovering the physics of unsteady flows in turbomachinery, such as blade row interactions, tip and hub clearance flows, hot streak migration in turbines, and end wall contouring. CFD, often regarded as the ”third way” aside from physical experiments and traditional theoretical analysis, is suitable to meet the challenges described above. The benefit of developing this high-fidelity unsteady CFD (Hi-Fi CFD) capability is threefold. First, it provides the fan/engine response assessment at an early stage of the engine development cycle to minimize performance surprises for new designs, and to help reduce engine re-test cost for new applications of existing engines. Secondly, CFD simulations can be used to improve existing one-dimensional models and to develop new reduced-order models as insights are gained regarding distortion transfer mechanisms and inner workings of fan response to various distortions. The bridge between the Hi-Fi CFD and the design practice needs to be built to realize the gains from the accumulated understanding of unsteady flow physics. Thirdly, it is an enabler of ”numerical experiments” for inlet-engine compatibility toward designing the inlet and the fan in a mutual flow field for new airframe initiatives such as uninhabited air vehicles and blended wing body commercial aircraft. The emphasis on high fidelity is driven by the fact that engine response to distorted flow represents the compressive turbomachinery aerodynamics in its fullest. It involves a large range of length and time scales of the flow and multiple disciplines in aero-thermodynamics.

Previous modeling efforts[6, 15, 16, 17] have largely focused on understanding the impact of inlet distortion on stall margin. The focus of this paper is on the pressure distortion induced swirl instead of a prescribed one at the fan face (aerodynamic interface plane, AIP). The numerical procedure is first validated against engine test data, and the simulation results are then analyzed to understand the flow physics of swirl distortion generation and transfer mechanism. Two different multi-stage fans, which represent different design philosophies, are considered in this study. The front block of the first fan and the rear block of the second fan are simulated respectively. The paper is divided into sections discussing the computational approach, the computational challenges and the analyses of the CFD results.

2 Computational Approach

This section describes the CFD flow solver, the selected fans and computational domains, and the boundary conditions at inlet and exit.

2.1 Flow Solver

The flow solver chosen was the unsteady RANS code, PTurbo,[18, 19] developed by Dr. Jenping Chen with support from NASA, Industry, and the DoD. Its solution algorithm is an implicit finite volume solver that incorporates Newton sub-iterations and a Block-Jacobi Gauss-Sidel relaxation scheme at each physical time step. It has a third-order accurate MUSCL-type of spatial discretization scheme coupled with a second order accurate temporal discretization, which helps to improve flow resolution and minimize dispersion error. Turbulence modeling is accomplished via the NASA/CMOTT k-epsilon model specifically developed for turbomachinery flows. This code was modified by GE to accept distortion boundary conditions at the inlet and exit boundaries. With pre-determined load balancing, this flow solver has demonstrated high scalability and parallel efficiency.

2.2 CFD Domain and Boundary Conditions for the First Fan

The entire first fan consists of three stages with an inlet guide vane (IGV). For the evaluation of computational approach, the simulation modeled the front block that includes the IGV and the first stage. This was deemed sufficient for the purpose of assessing the CFD prediction with a moderate requirement of computing resources. It also helped to identify and work out challenges with the CFD procedure. The computational domain consists of the full annulus of the IGV, Rotor-1 and Stator-1. The individual airfoil counts are: 13 IGVs, 24 Rotor-1 blades, and 62 Stator-1 vanes. The inlet total pressure was a one-per-rev sinusoidal distribution obtained from an engine test. The inlet total pressure and the exit static pressure boundary conditions are shown in Figure 1.

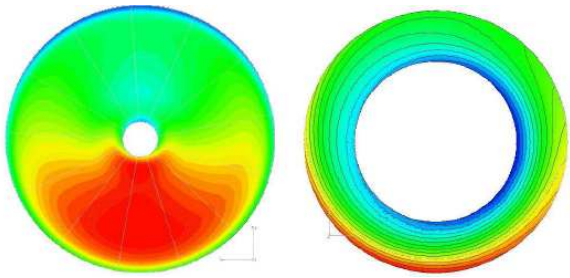

(a) Inlet total pressure **(b) S1 exit static pressure**

Figure 1. Boundary conditions of the first fan. (a) 1/rev total pressure distortion at the inlet. (b) Static pressure distribution at Stator-1 exit. (Red is high pressure, blue is low pressure. Top dead center is at 12 o'clock – fan rotates clockwise aft looking forward)

Figure 1a shows the absolute total pressure distribution at the inlet. Other inlet conditions, i.e. total temperature and flow angles were uniformly distributed across the circumference but with radial profiles. The exit boundary condition downstream of Stator-1 was more difficult to specify. The pressure distortion was not expected to attenuate at this location, and the engine test only had readings at the hub and the casing, with none in-between. The static pressure profile at this location was taken from the data-matched through flow solution of the engine test data, and was re-fitted with measurements from the hub and casing. The resulting exit boundary condition distribution is shown in Figure 1b. It is necessary to point out that the hub pressure probes were located within the hub cavity instead of being on the hub surface. This could drive the CFD prediction near the hub to a different flow pattern than expected.

2.3 CFD Domain and Boundary Conditions for the Second Fan

The second fan also consists of three stages with an IGV. For the second simulation, the computational domain consisted of three blade rows (Stator-2, Rotor-3, Stator-3) and a section of flow path downstream of Stator-3. Airfoil counts for the second fan were 108 Stator-2 vanes, 50 Rotor-3 blades, and 118 Stator-3 vanes. The inlet boundary conditions were developed from experimental data obtained with an 180/1rev inlet total pressure distortion on +10% high operating line. The inlet to this rear block of the fan has both total pressure and total temperature distortion. A sinusoidal function was fit through the Stator-2 leading edge data using equations 1 and 2.

$$Pt = Ptave * (1+amp\_Pt * \sin(phase\_Pt + \theta)) \quad (1)$$

$$Tt = Ttave * (1+amp\_Tt * \sin(phase\_Tt + \theta)) \quad (2)$$

The boundary condition was specified at 6 immersions (8.9%, 27.3%, 46.6%, 67%, 88.6%, and 94.3%). The amplitudes and phase are functions of the span. Contour plots of the inlet boundary condition for the second fan are shown in Figures 2a and 2b. Circumferentially uniform static pressure was specified (with a radial profile) at the exit boundary of the domain. The inlet pressure distortion is attenuated by the time it reaches this location. Each Stator-2 passage consisted of 153x57x73 nodes; each Rotor-3 passage consisted of

149x81x73 nodes and each Stator-3 passage had 215x57x73 nodes in the axial, tangential, and radial directions, respectively. 218,372,784 nodes were split into 444 blocks to run the simulation.

These two carefully selected computational domains are complementary to each other to cover a broader range in the effort of assessing the CFD capabilities.

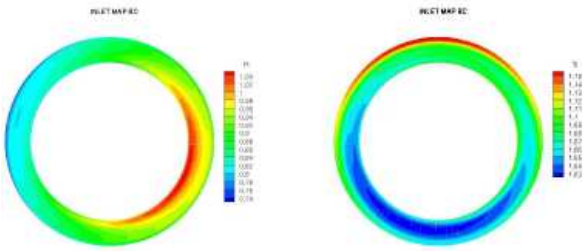

(a) **(b)**

Figure 2. Inlet boundary conditions of the second fan. (a) 1/rev total pressure distortion at inlet to Stator-2. (b) The total temperature distortion at inlet to Stator–2. (Red is high value and blue is low value).

3 Computational Challenges

The first challenge was to determine the appropriate level of details to resolve. The one-per-rev distortions have much longer wavelength than that of blade row interactions, and are inviscid in nature. This can be resolved using a fairly coarse grid. However, this is not the determining factor for the CFD fidelity level. Blade row interactions, wake migration, and viscous boundary layers must also be resolved properly because the imposed distortion interacts with all these high frequency perturbations in a highly non-linear fashion. On the other hand, the fidelity level is also limited by the computing resources and the required turn-around time. The stator row, which has most of the vanes, was used as a benchmark for grid resolution. A grid of 700,000 cells was determined to be appropriate to satisfy the above-mentioned criteria based on past time-accurate CFD experience and some trial calculations. This assessment was based on the third-order spatial accuracy of PTurbo. Grid density was then maintained for all other rows. Besides the regular clustering of cells in the viscous layers and in hub/tip clearance regions, special attention was taken to ensure proper grid resolution in the regions outside the viscous layers to resolve pressure and shock wave propagation. Smooth grid resolution was necessary in the circumferential direction near the vicinity of the sliding mesh interface to avoid interpolation errors. Furthermore, smooth grid resolution was also needed in the axial direction across the sliding mesh interface to minimize loss of flow features such as shock waves and wakes.

Several challenges related to the CFD flow solver were also addressed. The first is that the overall initial solution had to be a fairly good one, at least for the pressure distribution throughout the domain. This was achieved using the solution from GE's through-flow code, which provides an axi-symmetric solution. The other aspect is the marching from one time step to the next. The Newton iteration employed in the flow solver requires a close initial guess while providing rapid convergence. However, it is difficult to guarantee this everywhere in the flow field, especially in regions where flow properties have a large rate of change such as within the hub and tip clearances. This often led to an unexpected crash of the flow solver. A slight change of grid in those regions could help but that was on a trial-and-error basis. Intuitively, increase of grid density in those regions may help, but in reality it often made it worse. To alleviate this challenge, decreasing the physical time step proved helpful as the factorization error and linearization error in the LU-SGS procedure is directly linked to the size of the physical time step. In comparison to the alternative algorithm, dual-time stepping, in solving the unsteady RANS, the implicit LU-SGS procedure provides a nominal second-order accuracy in time derivatives, but often requires smaller physical time step than that can be tolerated by the dual-time stepping. Large time steps in the direct implicit algorithm would result in accumulation of those factorization and

linearization errors associated only with the implicit algorithm.

Yet another challenge was found when establishing the boundary conditions. The inlet and exit boundary condition treatment in today's CFD solvers still uses one-dimensional Riemann invariants based on characteristics of the flow equations, or the traveling direction of information from a physics perspective, determined by the eigen values of the inviscid Jacobian matrices of the flow equations. Flow reversal at the inlet and exit boundary would sooner or later cause a stability issue, simply because the reversed flow is not consistent with the characteristic based boundary condition treatment. On the other hand, non-reflecting boundary conditions for both the inlet and the exit are desired for this kind of calculations due to the lack of freedom to choose the location of the inlet and exit boundaries. It's either dictated by the underlying configuration or limited by the capability of the flow solver.

All the numerical simulations were carried out at the Aeronautical Systems Center, Major Shared Resource Center (ASC MSRC) running on an SGI Origin 3900 and SGI Altix Bx2.

4 CFD Results and Discussion

One of the objectives of this numerical study is to establish validated CFD capability for distortion transfer prediction. The details of the validation against engine test data of the two fans was presented in the aircraft engine committee panel session on "High Fidelity Engine Simulation" at the 2007 ASME / IGTI Turbo Expo in Montreal, Canada. The results and discussion in this paper focus primarily on the induced swirl and its transfer.

4.1 First Fan

Due to the circumferential inlet total pressure distortion, the inlet static pressure was distorted as well. This imbalance of static pressure drives a secondary flow that migrates from a high-pressure section to a low-pressure section along the circumference. This process induces an inlet swirl distortion that is quite visible upstream of the IGV, even though the inlet swirl boundary condition is held at zero uniformly. Figure 3 shows a snapshot of the time-resolved swirl and static pressure contour map at mid-span in an unwrapped blade-to-blade plane. The pressure-induced swirl is evident in the region upstream of the IGV.

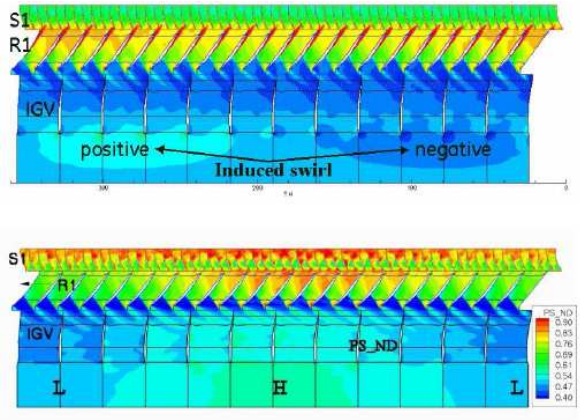

Figure 3. Induced swirl (top) and static pressure (bottom), snapshot of time-accurate solution at about 50% immersion

Figure 4 shows a few circumferential profiles of the swirl distribution at different axial locations starting from the domain inlet to the IGV exit. Driven by the static pressure imbalance in the circumference, the induced swirl develops gradually from the domain inlet, and near the leading edge of the IGV amounts to +/-5 degrees in a passage-averaged sense. This figure also shows that the existence of the IGV attenuates the induced swirl effectively. However, the swirl distortion is not completely attenuated by the IGV.

The amount of induced swirl distortion is different at various radial locations. Figure 5 shows the swirl distribution at mid-point between the IGV and the Rotor-1. Because the swirl is driven by the imbalance of the static pressure in the circumferential direction, it affects the most at lowest radius. So from the hub to the tip, one would expect the level of swirl distortion to be gradually reduced. Figure 5 shows this trend, except at 10% immersion.

This may be due to the tip clearance of the IGV, where the IGV's role in attenuating swirl distortion diminishes. However, the axial distance between the IGV and Rotor-1, which increases from the hub to the tip, might work against the trend shown in Figure 5. The pressure imbalance still exists in this region, and the longer axial distance near the tip would provide the tendency for the swirl distortion to be re-generated before it is ingested by Rotor-1.

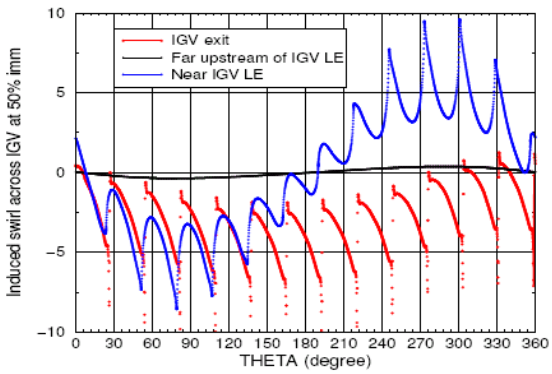

Figure 4. Induced swirl distribution upstream of the IGV and swirl attenuation across the IGV at 50% immersion.

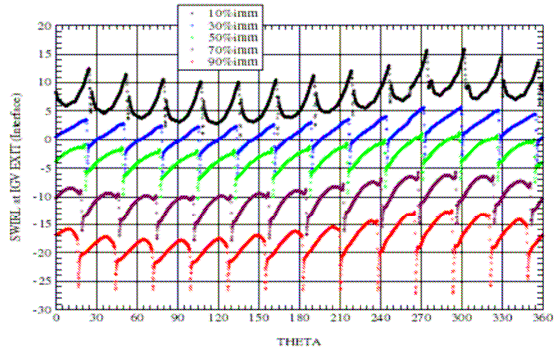

Figure 5. Induced swirl distribution at mid-point between the IGV and Rotor-1 at various radial locations (10, 30, 50, 70 and 90% immersions).

The induced swirl distortion is generally reduced as seen by Rotor-1 in the relative frame of reference. For two-dimensional flow, the transfer function of swirl angle from absolute reference frame (α) to relative reference frame (β) is as follows,

$$\tan\beta = \tan\alpha - \frac{1}{\lambda \cos\alpha} \qquad (3)$$

where, λ = V/U is the ratio of incoming absolute velocity (V) and wheel speed (U). This transfer function is plotted in Figure 6. In the [-30,30] range of commonly designed absolute swirl angles for rotors, the reduction rate is about 50% when λ = 1; more reduction when V is less than U, i.e. λ < 1; and less reduction when λ > 1. Recall, from Figure 4, that the even though IGV has attenuated the +/- 5 degrees of the swirl distortion, there is still +/-2 degrees of distortion delivered to Rotor-1, and it could still see an incidence swing of +/-1 degree during one revolution. A negative value of the incoming absolute swirl angle puts more load onto Rotor-1 relative to the condition of zero swirl as in undistorted flow, and correspondingly a positive swirl unloads Rotor-1. The swirl distortion is also evident downstream of Rotor-1 and Stator-1, as shown in Figure 7.

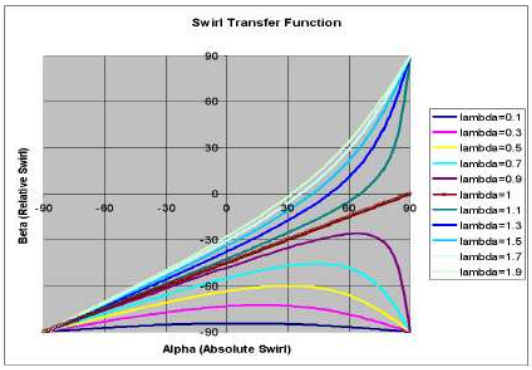

Figure 6. Swirl transfer function (Equation 3) from absolute frame to relative frame.

This swirl distortion has a different spatial phase (about 90 degrees) comparing to the distortion delivered by the upstream IGV. This might indicate that the swirl distortion downstream of Rotor-1 is not solely caused by the induced swirl upstream of Rotor-1. The flow pumping capability of Rotor-1, as a function of

circumferential location, is affected by other major factors. The incoming flow coefficient of Rotor-1, as a function of circumferential location, relates to the work coefficient affecting the turning of the flow across Rotor-1. The pressure distortion passing through Rotor-1 and the generation of the temperature distortion within Rotor-1 passage also affects Rotor-1's exit flow angle.

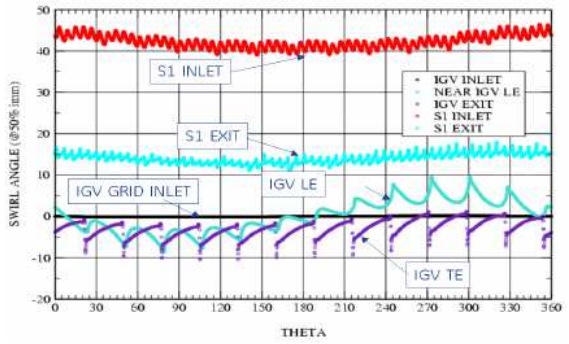

Figure 7. Swirl distortion transfer at 50% immersion.

As the flow passes through Stator-1, the stator seems to have a small role in attenuating the swirl distortion, as seen in Figure 7, though not as effectively as Rotor-1. While not shown herein, Stator-1 also plays a role in attenuating the total pressure distortion slightly. This could be attributed to the trading between the incidence swing and the aerodynamic loss relationship of a typical flow around stator vanes in turbomachinery.

4.2 Second Fan

The inlet total pressure and total temperature boundary conditions for the second fan were presented in Figure 2. The inlet swirl angle boundary condition varied with immersion but was constant circumferentially. Figure 8 shows the inlet and exit total pressure and temperature for 55% immersion from a previous analysis of total pressure distortion transfer and total temperature distortion generation.

An instantaneous snapshot of swirl and static pressure for the second fan near 50% immersion are shown in Figure 9. Similar to the first fan, a static pressure distortion results from the circumferential inlet total pressure distortion imposed at Stator-2 leading edge. This static pressure distortion is in phase with the total pressure distortion. Figure 9a shows a significant amount of swirl distortion is generated through Rotor-3.

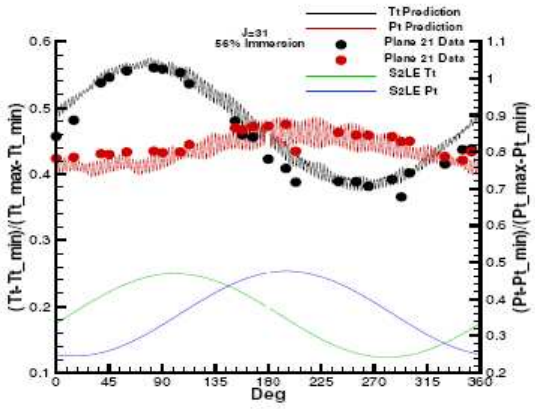

Figure 8. Comparison of the circumferential distribution of the total pressure and total temperature with data for the second fan near 50% immersion.

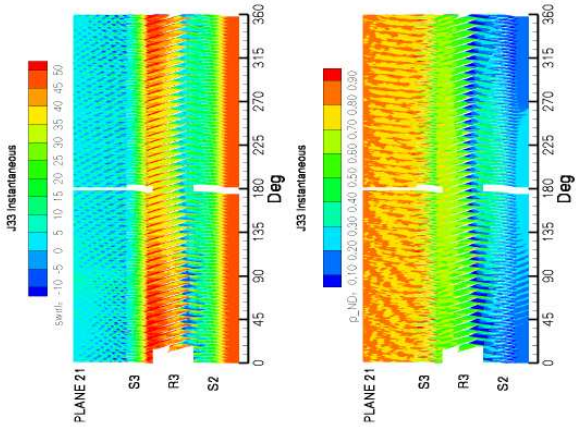

(a) Swirl **(b) Static Pressure**

Figure 9. Snap shot of time accurate solution for the second fan near 50% immersion. (Blue = -10 degrees of swirl or low pressure, Red = +50 degrees of swirl or high pressure).

Figure 10 shows the swirl determined from a time-average calculation for the entire circumference. Although there is significant variation in swirl across Stator-2 trailing edge pitch, a least squares fit shown in Figure 11 shows that there is no swirl distortion entering Rotor-3.

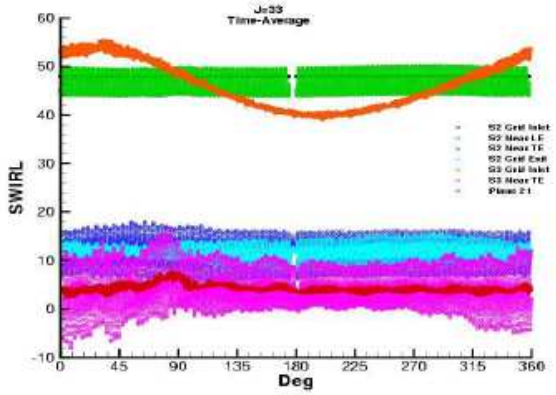

Figure 10. Swirl distortion transfer in the second fan near 50% immersion.

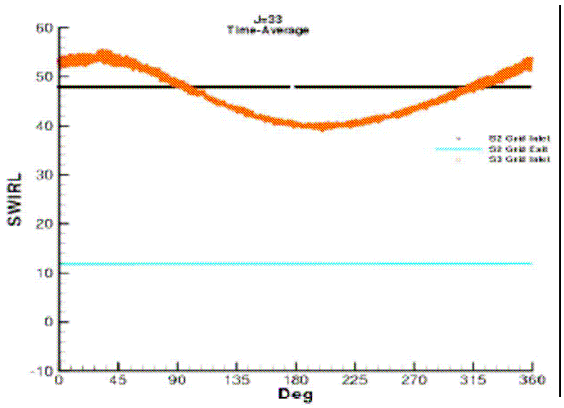

Figure 11. Swirl distortion generation in the second fan at 50% immersion.

Figures 10 and 11 clearly identify that the swirl distortion is generated through Rotor-3 resulting in a change in incidence into Stator-3 of 15 degrees. This is much larger than the swirl distortion generated in the first fan near the IGV leading edge (10 degrees) and through Rotor-1 (approximately 5 degrees). It is observed in the second fan that Stator-2 keeps any swirl distortion from being generated in that blade row but in Rotor-3 significant swirl distortion is generated. At Stator-3 exit there exists between 10 and 15 degrees variation in swirl across the vane passage but a least squares fit once again clarifies that there is very little swirl distortion at that location. It is observed that the larger variation in swirl across the passage corresponds to the low region of total pressure and static pressure distortion between 0 and 90 degrees and 270 to 360 degrees. At plane 21 where the exit static pressure boundary condition is applied there is no swirl distortion.

5 Concluding Remarks

Unsteady RANS calculations were successfully applied to predict the one-per-rev inlet total pressure distortion transfer in selected domains of two multi-stage fans. The following conclusions were drawn from the analyses of the numerical results with regard to the induced swirl distortion.

• An unsteady RANS CFD procedure was demonstrated by making use of High Performance Computing. No reduced order modeling was involved in this procedure. High Performance Computing allows full annulus simulations to be obtained in an acceptable time frame to be of benefit to the engine design process.

• The simulation of the front block of the first fan showed how swirl distortion was generated. The one-per-rev total pressure inlet distortion produced a static pressure distortion that drove the generation of swirl. The induced swirl distortion is found to reach its peak level near the leading edge of the IGV, and it has larger distortion level near hub due to the nature of the induction. The swirl distortion is attenuated effectively but not completely by the IGV. The remaining swirl distortion as seen by the rotor in the relative frame is still significant to affect the rotor loading. Rotor-1 itself, as it responds to the incoming total pressure distortion and induced swirl distortion, also produces a swirl distortion. This distortion is

observed to persist through the downstream Stator-1.

• The simulation of the rear block of the second fan shows that very high levels of swirl distortion can be generated in a rotor that sees a one-per-rev total pressure and total temperature distortion. The static pressure distortion drives this swirl generation even though no swirl distortion is present at the entrance to the rotor.

5 Acknowledgements

The authors wish to thank the support of the DoD High Performance Computing Modernization Program Office and the Aeronautical System Center Major Shared Resource Center for the Challenge Award that provided the high performance computing resources. The authors also want to thank Jenping Chen, now at Ohio State University, for his support of Pturbo. The authors are grateful for funding support provided by the Advanced Virtual Engine Test Cell (AVETeC). Finally, we thank the General Electric Company and the Air Force Research Laboratory Propulsion Directorate management for supporting the research and allowing the publication of this paper.

References

[1] Langston, C., "Distortion Tolerance – By Design Instead of By Accident," ASME Paper 69-GT-115, ASME, 1969.

[2] Mazzawy, R., "Multiple Segment Parallel Compressor Model for Circumferential Flow Distortion," *Transaction of the ASME, Journal of Engineering for Power*, April 1977, pp. 288–296.

[3] Roberts, F., Plourde, G., and Surakula, F., "Insights Into Axial Compressor Response To Distortion," AIAA Paper 68-565, AIAA, 1968.

[4] Reid, C., "The Response of Axial Flow Compressors to Intake Flow Distortion," ASME Paper 69-GT-29, ASME, 1969.

[5] Plourde, G. and Stenning, A., "The Attenuation of Circumferential Inlet Distortion In Multi-Stage Axial Compressors," AIAA Paper 67-415, AIAA 3rd Propulsion Joint Specialist Conference, Washington, D.C., July 1967.

[6] Hynes, T. and Greitzer, E., "A Method for Assessing Effects of Circumferential Flow Distortion on Compressor Stability," *Transactions of the ASME, Journal of Turbomachinery*, Vol. 109, July 1987, pp. 371–379.

[7] Chue, R., Hynes, T., Greitzer, E., Tan, C., and Longley, J., "Calculation of Inlet Distortion Induced Compressor Flow Field Instability," *Int. Journal of Heat and Fluid Flow*, Vol. 10, No. 3, September 1989, pp. 211–223.

[8] Cumpsty, N. A., Compressor Aerodynamics, Longman Group UK Ltd., London, England, 1989.

[9] Longley, J. P., "Measured and Predicted Effects of Inlet Distortion on Axial Compressors," ASME Paper 90-GT-214, 1990.

[10] Seddon, J., "Understanding and countering the swirl in S-ducts: tests on the sensitivity of swirl to fences," *Aeronautical Journal* , Vol. 88, April 1984, pp. 117–127.

[11] Pazur, W. and Flottner, L., "The Influence of Inlet Swirl Distortions on the Performance of a Jet Propulsion Two-Stage Axial Compressor," *Transactions of the ASME, Journal of Turbomachinery*, Vol. 113, April 1991, pp. 233–240.

[12] Longley, J. P. and Greitzer, E. M., "Inlet Distortion Effects in Aircraft Propulsion System Integration," Steady and Transient Performance Prediction of Gas Turbine Engines, AGARD-LS-183, 1992.

[13] Govardhan, M. and Viswanath, K., "Effect of circumferential Inlet flow distortion and swirl on the flow field of an axial flow fan stage," ASME Paper 96-GT-263, 1996.

[14] Cousins, W., "History, Philosophy, Physics, and Future Directions of Aircraft Propulsion System/Inlet Integration," ASME Paper GT-2004-54210, 2004.

[15] Gong, Y., "A Computational Model for Rotating Stall Inception and Inlet Distortions in Multistage Compressor," Ph.D. Dissertation, Massachusetts Institute of Technology, 1998.

[16] Hale, A., Davis, M., and Sirbaugh, J., "A Numerical Simulation Capability for Analysis of Aircraft Inlet – Engine Compatibility," ASME Paper GT-2004-53473, 2004.

[17] Chima, R. V., "A Three-Dimensional Unsteady CFD Model of Compressor Stability", ASME Paper GT2006-90040, 2006.

[18] Chen, J. P. and Celestina, M. L., "A New Procedure for Simulating Unsteady Flows Through Turbomachinery Blade Passages", ASME Paper 94-GT-151, 1994.

[19] Chen, J. P. and Briley, W. R., "A Parallel Flow Solver for Unsteady Multiple Blade Row Turbomachinery Simulations", ASME Paper GT2001-0348, 2001.

Copyright Statement